

Role of electronic structure on nitrate reduction to ammonium: a periodic journey

O. Quinn Carvalho,^{1,2} Rylee Marks,¹ Hoan K.K. Nguyen,¹ Molly E. Vitale-Sullivan,³ Selena C. Martinez,¹ Líney Árnadóttir,¹ Kelsey A. Stoerzinger^{1,4,z}

¹ School of Chemical, Biological and Environmental Engineering, Oregon State University, Corvallis, OR, 97331, USA

² The Advanced Light Source, Lawrence Berkeley National Laboratory, 1 Cyclotron Road, Berkeley, CA 94705, USA

³ School of Mechanical, Industrial, and Manufacturing Engineering, Oregon State University, Corvallis, OR, 97331, USA

⁴ Physical and Computational Sciences Directorate, Pacific Northwest National Laboratory, 902 Battelle Blvd. Richland, WA 99354, USA

^z Corresponding email: kelsey.stoerzinger@oregonstate.edu

1 **1. Abstract**

2 Electro catalysis is a promising approach to convert waste nitrate to ammonia and help
3 close the nitrogen cycle. This renewably-powered ammonia production process sources
4 hydrogen from water (as opposed to methane in the thermal Haber-Bosch process), but requires
5 a delicate balance between a surfaces' activity for the hydrogen evolution reaction (HER) and
6 the nitrate reduction reaction (NO₃RR), influencing Faradaic efficiency (FE) and selectivity to
7 ammonia/ammonium over other nitrogen-containing products. We measure ammonium FEs
8 ranging from 3.6±6.6% (on Ag) to 93.7±0.9% (on Co) across a range of transition metals (TMs;
9 Ti, Fe, Co, Ni, Ni_{0.68}Cu_{0.32}, Cu, and Ag) in buffered neutral media. To better understand these
10 competing reaction kinetics, we develop a microkinetic model that captures the voltage-
11 dependent nitrate rate order and illustrates its origin as competitive adsorption between nitrate
12 and hydrogen adatoms (H^{*}). NO₃RR FE can be described via competition for electrons with
13 the HER, decreasing sharply for TMs with high work function and correspondingly high HER
14 activity (e.g. Ni). Ammonium selectivity nominally increases as TM d-band center energy (E_d)
15 approaches and overcomes the Fermi level (E_F), but is exceptionally high for Co compared to
16 materials with similar E_d . Density functional theory (DFT) calculations indicate Co maximizes
17 ammonium selectivity via (1) strong nitrite binding enabling subsequent reduction and (2)
18 promotion of nitric oxide dissociation, leading to selective reduction of the nitrogen adatom
19 (N^{*}) to ammonium.

20

1 2. Introduction

2 Nitrate accumulation represents a growing threat to global drinking water resources and
3 human health.¹ At the same time, ammonia production (the largest anthropogenic disruption to
4 the nitrogen cycle)² emits more carbon dioxide than production of any other commodity
5 chemical.³ Together, this motivates research in technologies that can generate green ammonia,
6 preferably circularly by upgrading waste forms of nitrogen.⁴ Electrochemical reduction offers
7 a scalable, distributable, and increasingly economical⁵ technology for the upgrading of waste
8 nitrate to value-added products (ammonium⁶⁻⁸ and hydroxylamine⁹) or benign dinitrogen gas.¹⁰

9 Nitrate reduces to ammonium by a complex 8-electron and 10-proton process. In the rate-
10 limiting step, adsorbed nitrate reduces to nitrite.¹⁰ Nitrite is the predominant side product in
11 neutral and alkaline electrolytes,¹¹⁻¹⁵ reducing further to nitric oxide when remaining adsorbed
12 on the surface (and more complex products when present in the aqueous phase¹⁶). Nitric oxide
13 serves as a critical intermediate in determining selectivity between nitrogen/oxides and
14 ammonium or hydroxylamine.¹⁷ Mechanistically, adsorbed nitric oxide (NO^*) forms
15 ammonium by one of two pathways: (1) Eley-Rideal like proton-coupled electron transfer
16 (PCET) reducing NO^* to hydroxylamine (NH_2OH^*) and further to ammonium;¹⁸ or (2)
17 dissociation of NO^* into N^* and O^* adatoms and subsequent Langmuir-Hinshelwood like
18 hydrogenation of N^* by H^* to ammonium.^{10,19}

19 Despite these complexities, recent electrochemical NO_3RR literature has demonstrated
20 appreciable FE and selectivity to ammonia in highly alkaline electrolytes. For example,

1 strained Ru nanoparticles—where Ru^{20,21} is a benchmark thermal Haber Bosch catalyst—have
2 achieved 100% FE at potentials as cathodic as -0.2 V vs the reversible hydrogen electrode
3 (RHE), albeit at high nitrate concentrations (1 M).⁶ First row transition metals such as Co^{22,23}
4 and alloys including NiCu⁷ have also demonstrated high FE. However, while such examples
5 exist under alkaline pH, a fundamental understanding of the physicochemical factors driving
6 NO₃RR selectivity towards ammonium is lacking, particularly in the circumneutral pH range
7 expected of most wastewaters.^{8,24,25}

8 Here we investigate electrocatalytic NO₃RR activity and selectivity at low conversion for
9 a series of polycrystalline 3d (Ti, Fe, Co, Ni, Ni_{0.68}Cu_{0.32}, and Cu) and 4d¹⁰ (Ag) transition
10 metal foils (TMs) in buffered sodium phosphate electrolyte (pH 7; Na_xH_{3-x}PO₄). Trends
11 between phosphate-mediated HER activity and H chemisorption energy²⁶ correspond with the
12 familiar Sabatier relationship between HER exchange current and metal-H* bond strength,^{27,28}
13 providing an *in-situ* probe of H* affinity for different TM surfaces. Microkinetic modeling of
14 the competition between the HER and NO₃RR captures experimentally observed potential-
15 dependent nitrate rate order, where peak rate order magnitude and potential are well-described
16 by the difference in H* and nitrate adsorption free energies ($\Delta G_{H^*} - \Delta G_{NO_3^-}$). The HER and
17 NO₃RR compete for electrons, where HER activity descriptors (TM work function by
18 photoemission²⁹ and H chemisorption energy^{26,28}) play key roles in describing NO₃RR FE. The
19 d-band model³⁰ provides a fundamental understanding of the relationship between TM
20 electronic structure and nitric oxide adsorption energies, describing to a first order the increased

1 selectivity towards ammonium as the TM E_d approaches E_F . Selectivity can be further
2 explained by the differences in calculated reaction free energies for nitrite reduction
3 ($\Delta G_{NO^*} - \Delta G_{NO_2^-}$) and nitric oxide dissociation ($\Delta G_{N^*+O^*} - \Delta G_{NO^*}$), where Co is an optimal
4 catalyst for both of these selectivity-critical reaction steps. Together, the physicochemical
5 parameters of work function, H chemisorption energy, and E_d vs E_F provide intrinsic
6 electrocatalyst design parameters for the selective production of green-ammonium from waste
7 nitrate.

8

9 **3. Methods**

10 We quantify the formation of nitrite and ammonium, the two primary products at the pH
11 and low conversions measured here,¹¹⁻¹⁵ over a series of commercial polycrystalline TM foils
12 at a range of potentials as detailed in the Supplemental Information (SI). To better control
13 nitrate conversion as a variable, a fixed charge is passed per nitrate anion (0.2 or 0.04 e^-/NO_3^-),
14 corresponding to maximum 10 or 2% conversion of nitrate assuming 100% FE towards nitrite.
15 Additional methodologies for activity, selectivity, and DFT calculations are provided in the SI.

16

17 **4. Results**

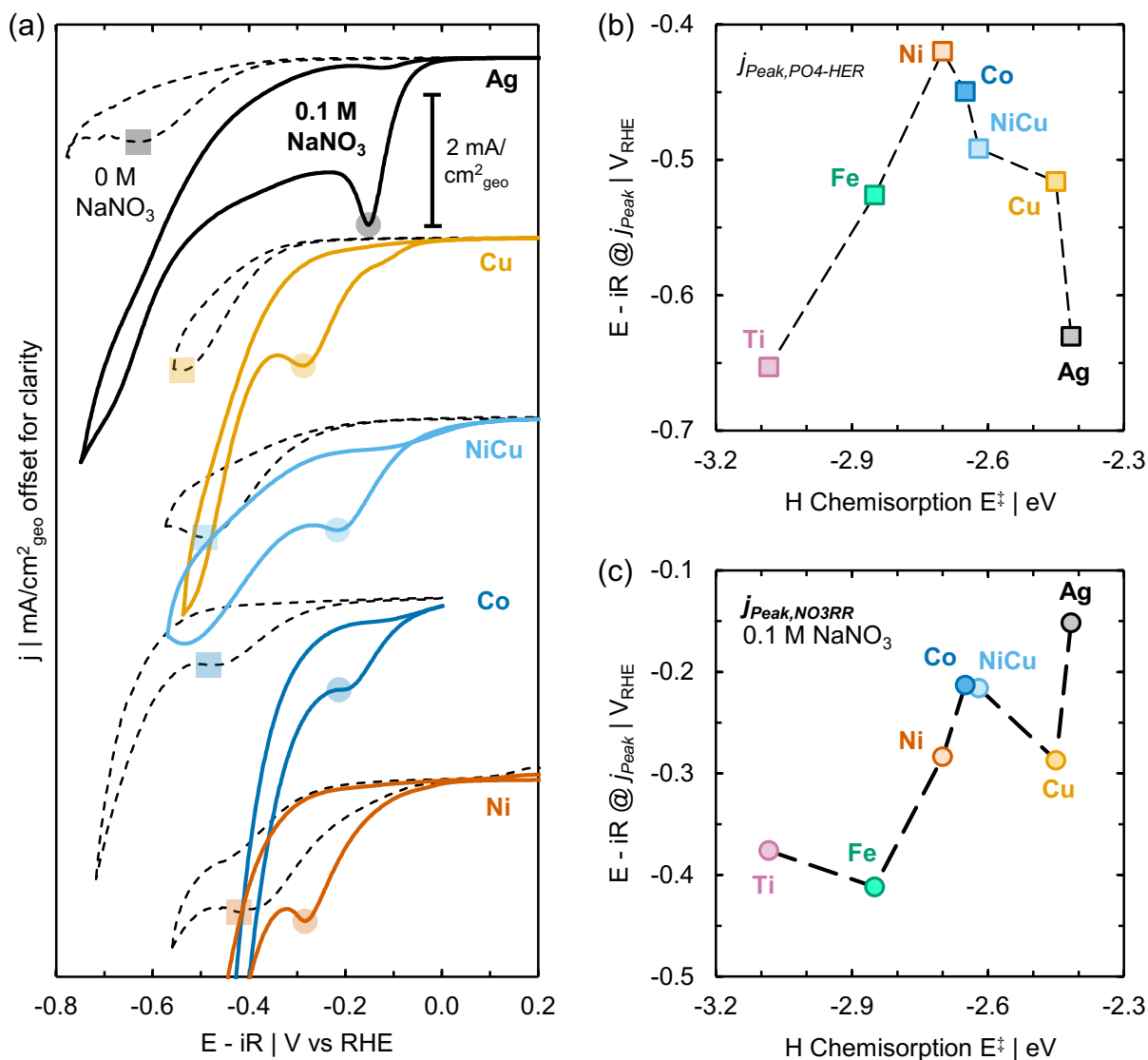
18 *4.1. Role of H chemisorption energy and HER on NO_3RR activity*

19 We first probe the ability of TM foils to abstract protons from phosphate anions with cyclic
20 voltammetry (CV, Figure 1a and S1). Phosphate-mediated HER (Figure 1a, black dashed lines)

1 is observed as a mass-transfer limited peak at potentials less-cathodic than water-dissociation
2 (Figures S1 and S2), where protons are easier to extract from phosphate anions than from
3 water.³¹ The comparable mass-transfer limited current density (ca. 2 mA/cm²_{geo}; Figure S1)
4 across TMs indicates similar roughness except for the lower-roughness Ag and Co.

5

6



1
 2 Figure 1. (a) CV collected at 10 mV/s in quiescent 0.1 M Na_xH_{3-x}PO₄ in the absence (dashed black trace) and
 3 presence (solid colorful trace) of 0.1 M NaNO₃ for denoted TM foils. CVs offset for clarity with mass-transfer
 4 limited phosphate-mediated HER (squares) and nitrate reduction (circles) denoted. Potential at mass-transfer
 5 limited (b) phosphate-mediated HER ($E - iR @ j_{Peak, PO4-HER}$) and (c) nitrate reduction ($E - iR @ j_{Peak, NO3RR}$) in the
 6 presence of 0.1 M NaNO₃, both plotted against H chemisorption energy from Ref. 26. $E - iR @ j_{Peak, NO3RR}$ for Co
 7 and Fe are from inflection points (minimum in differential current with respect to voltage) as surrogate for
 8 potential at peak current. Data for H chemisorption energy adapted from Ref. 26 and interpolated for Ni_{0.68}Cu_{0.32}
 9 (denoted as light blue NiCu) as the sum of molar fractions from Ni and Cu.

10

11 The potential at peak phosphate-mediated HER ($E - iR @ j_{Peak, PO4-HER}$; squares in Figure
 12 1a) exhibits a volcano-style trend with literature H chemisorption energies (Figure 1b),

1 mirroring the well-known relationship between HER exchange current and H chemisorption
2 energy in acidic electrolytes (Figure S3a).^{26–28} HER activity on TMs binding H weakly (e.g.
3 Ag, Cu) is limited by proton adsorption, while TMs binding H strongly (e.g. Fe, Ti) are limited
4 by H-H bond formation kinetics.³² HER activity is also well-described by work function,²⁹
5 where higher work function TMs (e.g. Ni and other Group X TMs) demonstrate greater HER
6 activity than those of lower work function TMs (Figure S3b).²⁸

7 For CVs in the presence of 0.1 M sodium nitrate (Figure 1a, solid lines), nitrate reduction
8 current becomes apparent at potentials nominally less-cathodic than HER (Figures S4 and S5).
9 NO₃RR current manifests as either a shift in the phosphate deprotonation peak to less cathodic
10 potentials (e.g. Ni), or as a second mass-transfer limited peak (e.g. Ag). A Nernstian shift in
11 peak potentials to less-cathodic potentials occurs with increasing logarithmic nitrate
12 concentration (Figure S6).

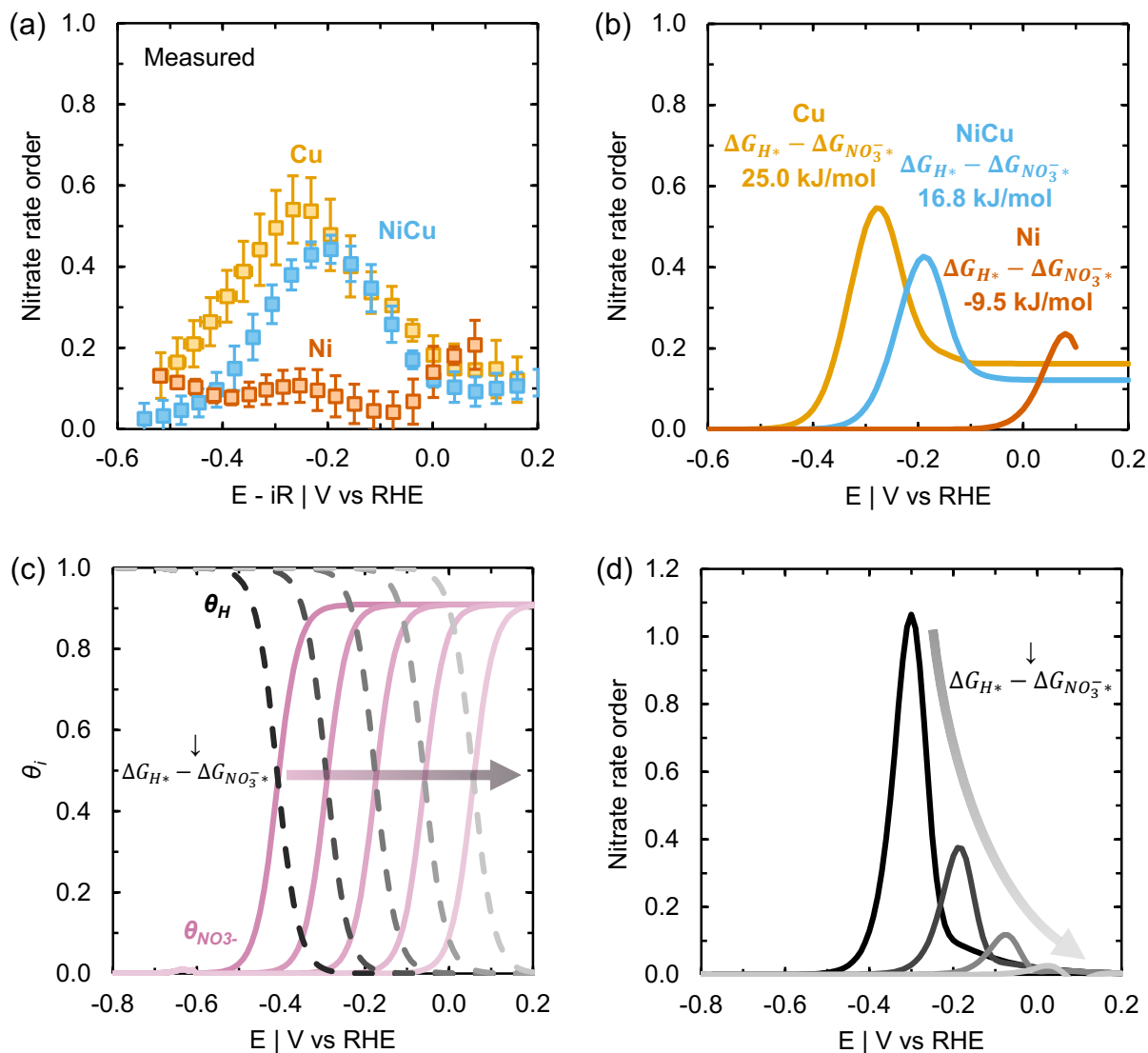
13 For first-row (3d) TMs, mass-transfer limited nitrate reduction potentials (Figure 1c, E –
14 $iR @ j_{Peak,NO3RR}$) are the least-cathodic for TMs binding H* slightly weaker than Ni (e.g. Co and
15 Ni_{0.68}Cu_{0.32}). Alloying weak H*-binding Cu with Ni (e.g. Ni_{0.68}Cu_{0.32}, denoted NiCu) also shifts
16 NO₃RR onset to less-cathodic potentials than either terminal monometallic composition,
17 consistent with literature in alkaline electrolyte.⁷ In contrast, TMs binding H* strongly (e.g. Fe,
18 Ti) have considerably more-cathodic mass-transfer limited nitrate reduction potentials (Figure
19 1c and S6), suggesting that strong H chemisorption energy leads to sluggish PCET and
20 hydrogenation kinetics for the NO₃RR.

1
2
3
4
5
6
7
8
9
10
11
12
13
14
15
16
17
18
19
20

4.1.1. Microkinetic modeling of potential-dependent nitrate rate order

We next measure nitrate rate order experimentally (Figures S7 and S8) and develop a microkinetic model demonstrating the impact of competition between nitrate and H^* on NO_3RR activity (Figure 2). This model describes how thermodynamic and kinetic parameters drive the rate-limiting steps of the HER³³ and NO_3RR . Here we highlight modelling results of three TMs along the weak H chemisorption arm of Figure 1b (*e.g.* Cu, Ni, and $Ni_{0.68}Cu_{0.32}$, see SI for model details and experimental nitrate rate order for additional TMs, Figure S8).

For TMs binding H^* weakly (Figure 1b), nitrate rate order exhibits a potential-dependent peak (Figure 2a), reminiscent of a competitive Langmuir-Hinshelwood mechanism.³⁴ We therefore hypothesize that this peak shape originates from competitive adsorption between H^* and nitrate. Increasing H chemisorption energy corresponds to a decreased peak rate order magnitude and shift to less-cathodic potentials. These experimental rate-order profiles are well-described by our microkinetic model (Figure 2b), assuming reduction of adsorbed nitrate to nitrite is rate limiting (via sequential PCET and/or hydrogenation, equations S19-S21)¹⁰ and describing HER kinetics (equations S7-S15) following the work of Shinagawa *et al.*³³ Agreement between experimental (Figure 2a) and modeled (Figure 2b) nitrate rate order versus potential can be achieved by changing only the thermodynamic parameters reflecting the difference in $\Delta G_{H^*} - \Delta G_{NO_3^-}$ ($\propto -\log[K_H/K_{NO_3^-}]$), where $\Delta G_{H^*} - \Delta G_{NO_3^-}$ of Cu is greater (lower relative H^* affinity, Figure 1b) than that of $Ni_{0.68}Cu_{0.32}$ and Ni.



1
2 Figure 2. (a) Experimentally measured and (b) microkinetically modelled potential-dependent nitrate rate order,
3 measured by steady-state chronoamperometry in 0.1 M $Na_xH_{3-x}PO_4$ with a series of sodium nitrate concentrations
4 (Figure S7) for Cu (golden), $Ni_{0.68}Cu_{0.32}$ (light blue), and Ni (orange). Error bars in (a) denote one standard
5 deviation from the average of at least three ($n = 3$) separate measurements. Only thermodynamic parameters
6 ($\Delta G_{H^*} - \Delta G_{NO_3^-}$) in (b) are adjusted as denoted to achieve agreement; see Table S1 for additional model
7 parameters. (c) Potential-dependent fractional H^* (black dashed) and nitrate (fuchsia solid) coverage for a series
8 of H^* to nitrate adsorption coefficients ($K_H:K_{NO_3}$) denoted by increasingly light shades in order of 10^{-7} , 10^{-5} , 10^{-3} ,
9 10^{-1} , and 10^1 . (d) Nitrate rate order for a series of $K_H:K_{NO_3}$ denoted by increasingly light shades of grey in order
10 of 10^{-5} , 10^{-3} , 10^{-1} , and 10^1 .

11

12 The potential at maximum rate order ($E_{max\ rate}$) serves as a direct indicator of $\Delta G_{H^*} -$

1 $\Delta G_{NO_3^-}$ for TM surfaces (Figure S13). Potential-dependent nitrate coverage is implicitly
 2 derived from a competitive adsorption isotherm with H^* (equations S13 and S18; Figure 2c).
 3 At potentials where H^* coverage is low ($E \gg HER$), modeled nitrate coverage is defined by
 4 the material-dependent nitrate adsorption coefficient ($K_{NO_3^-}$) and the activity of solution-phase
 5 nitrate anions ($\alpha_{NO_3^-}$, approximated here as concentration; equation S18). H^* , having explicitly
 6 potential-dependent coverage (equation S13), displaces nitrate at increasingly cathodic
 7 potentials, where the potential with equivalent H^* and nitrate coverage ($\theta_H = \theta_{NO_3^-}$) is
 8 proportional to $\Delta G_{H^*} - \Delta G_{NO_3^-}$ (Figure S10). Further, $E_{max\ rate}$ coincides with the potential
 9 where $\theta_H = \theta_{NO_3^-}$ (Figure S10), providing optimal reactant coverages to facilitate Langmuir-
 10 Hinshelwood-like nitrate reduction mechanisms (equations S20 and S21). As the potential
 11 where $\theta_H = \theta_{NO_3^-}$ shifts cathodically with increasing $\Delta G_{H^*} - \Delta G_{NO_3^-}$ (Figure 2c), rate order
 12 magnitude increases (Figure 2d) due to the exponential dependence of nitrate reduction on
 13 overpotential (equations S19-S21, Figure S13c). This provides a physical interpretation of why
 14 $\Delta G_{H^*} - \Delta G_{NO_3^-}$ dictates both $E_{max\ rate}$ and rate order magnitude, while the ratio of kinetic
 15 parameters (reaction rate constants; $k_{NO_3RR}:k_{HER}$) only controls magnitude (Figure S13b).

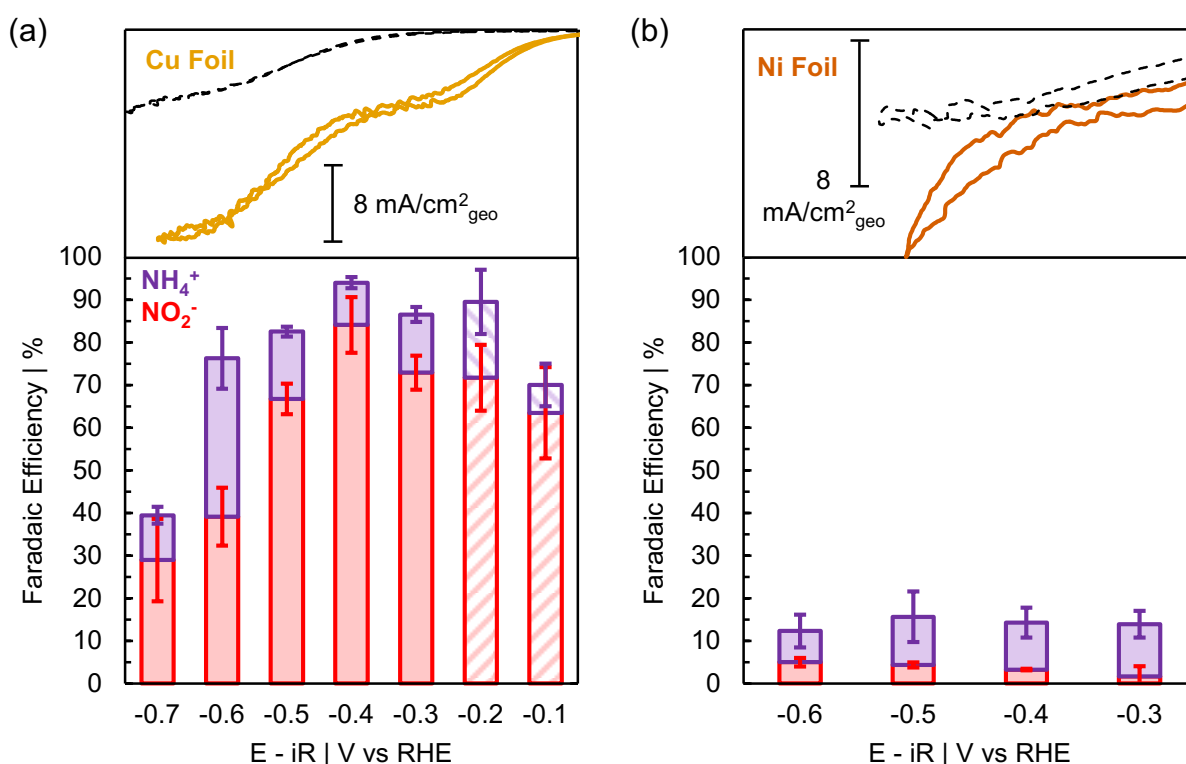
16

17 *4.2. NO₃RR FE and selectivity to ammonium: dependence on bulk electronic structure*

18 We first introduce potential-dependent NO₃RR FE and ammonium selectivity data for Cu
 19 and Ni foils (Figure 3), expanding to include the role of alloying in this system (Figure 4) and
 20 additional monometallic TMs (Figures 5 and 6). Cu demonstrates appreciable (>70%) NO₃RR

1 FE at potentials prior to the onset of water-dissociative HER (> -0.6 V vs RHE; Figure 3a).
 2 Within this range of potentials, the majority of charge passed to nitrate results in formation of
 3 nitrite with a minority fraction designated to ammonium formation (*ca.* 10-20%). However, the
 4 onset of water-dissociative HER (CV at top of Figure 3a) increases selectivity towards
 5 ammonium at the expense of total NO_3RR FE (≤ -0.6 V vs RHE), suggesting elevated H^*
 6 coverage mediates hydrogenation of reduced nitrogenous species ($\text{NO}_{x,\text{ads}}$).

7



8
 9 Figure 3. Top: CVs of (a) Cu and (b) Ni collected at 10 mV/s in stirred $0.1 \text{ M Na}_x\text{H}_{3-x}\text{PO}_4$ in the absence
 10 (dashed black lines) and presence (solid lines) of 0.1 M NaNO_3 . Top of panel denotes $0 \text{ mA/cm}^2_{\text{geo}}$ with 8
 11 $\text{mA/cm}^2_{\text{geo}}$ scale bar for reference. Bottom: FE to nitrite (red bars) and ammonium (purple bars) for (a) Cu and
 12 (b) Ni foils after passing 0.2 (solid) or $0.04 \text{ e}^-/\text{NO}_3^-$ (hatched) by 85% iR -corrected chronoamperometry in
 13 stirred $0.1 \text{ M Na}_x\text{H}_{3-x}\text{PO}_4$ with 0.1 M NaNO_3 . Error bars denote one standard deviation of the average of at least
 14 three ($n = 3$) separate measurements.

15

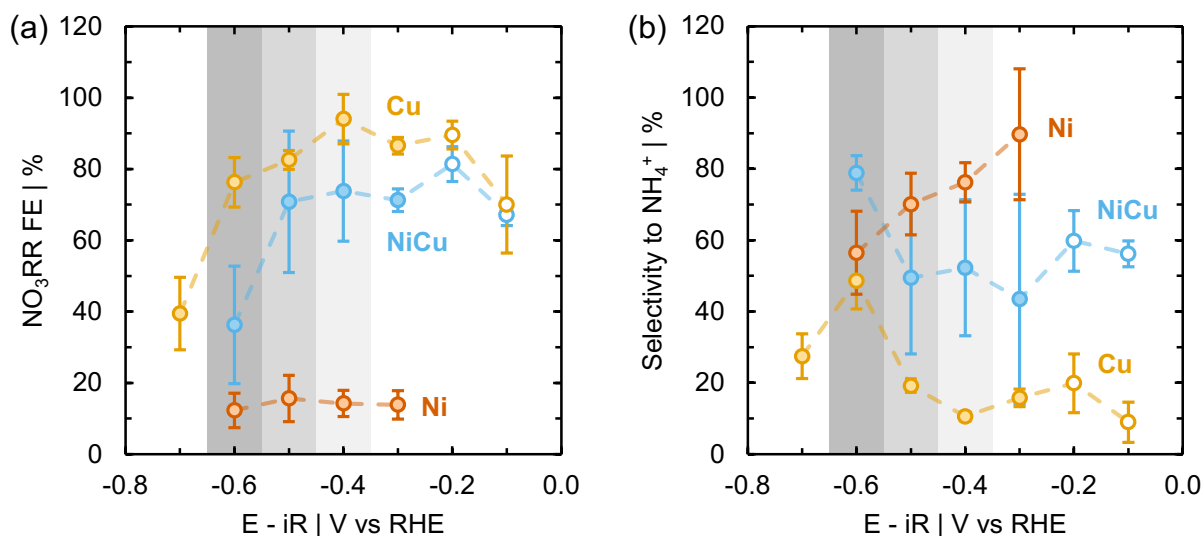
1 In contrast to Cu, Ni demonstrates poor NO₃RR FE (10-15%) across the range of potentials
2 measured here (Figure 3b). A qualitative assessment of CVs in stirred electrolyte (top panels
3 of Figure 3) reinforce this observation, where the ratio of current in the presence and absence
4 of nitrate on Ni is much lower than that of Cu. However, electrons contributing to NO₃RR on
5 Ni primarily form ammonium (50-90%). Ammonium selectivity on Ni decreases with
6 increasingly cathodic potentials, unlike all other TMs measured here (Figures S16 and S17).
7 This suggests adsorbed H* are more likely to form dihydrogen than to hydrogenate nitrate as
8 cathodic potential is increased, or that mass-transfer limited phosphate deprotonation (top panel
9 of Figure 3b) hinders the formation of proton-rich ammonium (10 H⁺/NH₄⁺ from nitrate).

10 As discussed in the Introduction section, the ammonium-formation mechanism abides by
11 one of two pathways: PCET of associatively-adsorbed NO* (Ref. 18) or dissociative adsorption
12 of nitric oxide and subsequent hydrogenation of N* adatoms by H*.^{10,19} Activation of a
13 Langmuir-Hinshelwood like NO* hydrogenation pathway (e.g. NO* + H*) may explain the
14 source of enhanced ammonium selectivity on Cu at HER-relevant potentials. Nitric oxide
15 adsorbs associatively on low H* chemisorption energy Cu (Figure S18),^{35,36} where ammonium
16 formation by PCET is likely predominant, only activating the Langmuir-Hinshelwood
17 mechanism after appreciable H* coverage is achieved (e.g. cathodic of HER onset). In contrast,
18 Ni— preferring dissociative^{35,36} nitric oxide adsorption—likely only forms ammonium by a
19 Langmuir-Hinshelwood like N* adatom hydrogenation, where our rate-order analysis and
20 microkinetic modelling indicate high H* affinity at all potentials measured here.

1
2
3
4
5
6
7
8
9
10
11
12
13
14
15

4.2.1. Tailoring electronic structure towards ammonium selectivity by alloying

Motivated by the high ammonium selectivity of Ni and NO₃RR FE of Cu, we next consider the FE and selectivity of a Ni_{0.68}Cu_{0.32} alloy. In circum-neutral electrolyte, Ni_{0.68}Cu_{0.32} foil demonstrates potential-dependent NO₃RR FE (Figure 4a), and selectivity towards ammonium (b), nominally intermediate of the two terminal compositions (e.g. Cu and Ni). Similar to Cu, Ni_{0.68}Cu_{0.32} demonstrates appreciable (*ca.* 70-80%) FE at potentials less-cathodic than the onset of HER (>-0.6 V_{RHE}), though has much greater selectivity towards ammonium (*ca.* 40-60%) at comparable potentials. Selectivity towards ammonium increases at the expense of FE with the onset of HER (-0.6 V_{RHE}), similar to observations on Cu of potential-dependent competition between nitrate reduction intermediates and H* for surface sites and NO₃RR and HER for electrons. Note, the larger error bars of Ni_{0.68}Cu_{0.32} relative to Ni or Cu may result from differences in surface composition resultant from surface preparation (see SI methods).



1
 2 Figure 4. (a) NO₃RR FE and (b) ammonium selectivity for Cu (golden), Ni (orange), and Ni_{0.68}Cu_{0.32} (light blue)
 3 measured by 85% iR-corrected chronoamperometry to 0.2 (closed) or 0.04 (open symbols) e⁻/NO₃⁻ in stirred 0.1
 4 M Na_xH_{3-x}PO₄ with 0.1 M NaNO₃. Shaded bars denote the potential window where HER becomes competitive
 5 with NO₃RR, and is used to compare NO₃RR FE and selectivity to ammonium for all TMs in Figures 6 and 7.
 6 Error bars denote one standard deviation of the average of at least three (n = 3) separate measurements.

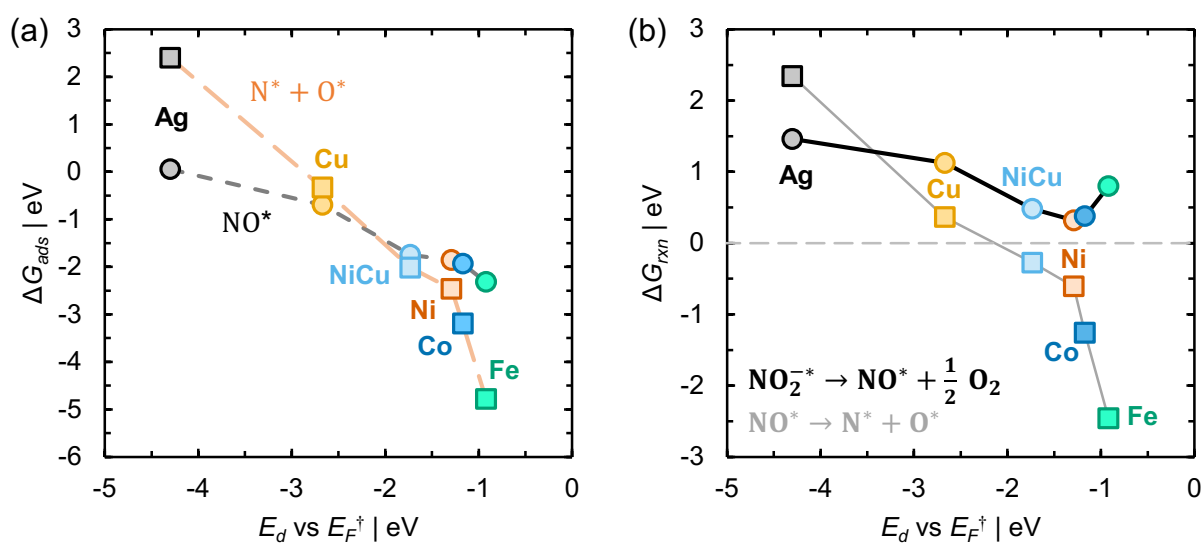
7

8 4.2.2. Dependence of intermediate adsorbate energy on TM electronic structure

9 We propose selectivity towards ammonium is greater on surfaces favoring dissociative
 10 nitric oxide adsorption and subsequent N* adatom hydrogenation by H* (Figure 3 and 4). Here
 11 we discuss the relationship between nitric oxide adsorption and dissociation energies and TM
 12 electronic structure by DFT. We limit our discussion to elements in metallic state under the
 13 NO₃RR conditions considered here, with consideration of Ti (uncertain surface oxidation
 14 state)^{37,38} in the SI (Table S3).

15 Our theoretical calculations identify nitric oxide free energy of adsorption (ΔG_{NO^*})
 16 becomes more negative as TM E_d approaches E_F (Figure 5a), in-line with descriptions of other
 17 simple adsorbates.^{30,39,40} Dissociation activation barriers decrease with reaction enthalpy

1 ($\Delta(E_{N^{*+O^*}} - E_{NO^*}))$ and E_d vs E_F (Figure S22), in-line with Brønsted-Evans-Polanyi (BEP)
 2 scaling relationships.^{36,41} This suggests preferential associative adsorption on weak-binding
 3 TMs (e.g. Ag and Cu; $\Delta G_{NO^*} < \Delta G_{N^{*+O^*}}$) and dissociative adsorption on strong-binding TMs
 4 (e.g. Ni_{0.68}Cu_{0.32}, Ni, Co, and Fe; $\Delta G_{NO^*} > \Delta G_{N^{*+O^*}}$), in line with prior literature on stepped
 5 surfaces (Figure S18) and *in vacuo* single crystal adsorption studies.^{35,36} Assuming N* can only
 6 be hydrogenated to ammonium as a terminal reduction product, this increased preference
 7 towards dissociative nitric oxide adsorption could lead to enhanced selectivity towards
 8 ammonium on TMs where E_d approaches and overcomes E_F .



10
 11 Figure 5. (a) Free energy of associative (circles with short black dashes) and dissociative (squares with long orange
 12 dashes) nitric oxide adsorption against E_d vs E_F for denoted TM surfaces. (b) Reaction free energies (ΔG_{rxn}) of
 13 nitrite reduction to nitric oxide (circles with thick black lines) and nitric oxide dissociation (squares with thin grey
 14 lines) against E_d vs E_F for denoted TMs. Dashed grey line in (b) denotes zero reaction free energy for clarity. The
 15 lowest energy surfaces for each crystal structure were used for calculation: fcc(111), bcc(110), or hcp(0001).^{42 †}
 16 Data for E_d vs E_F adapted from Ref. 30.

17

1 Understanding the material-dependent driving force for nitrite (the predominant NO₃RR
2 side-product in neutral and alkaline electrolytes)^{11–15} reduction may shed further light on trends
3 in ammonium selectivity. We next compare the calculated free energy difference between
4 nitrite and nitric oxide ($\Delta(G_{NO^*} - G_{NO_2^-*})$, Figure 5b circles). Deoxygenation is assumed to
5 occur by PCET common across all catalysts and is treated here by including $\frac{1}{2}$ O₂ as a product
6 in the reaction free energy difference; i.e. $NO_2^{*} \rightarrow NO^* + \frac{1}{2} O_2$. The free energy of nitrite
7 adsorption ($\Delta G_{NO_2^-*}$) scales with both that of associative (ΔG_{NO^*}) and dissociative
8 ($\Delta G_{N^*+O^*}$) nitric oxide adsorption (Figure S23), in-line with scaling relationship for molecules
9 of similar functionality.⁴³ As E_d approaches E_F , $\Delta(G_{NO^*} - G_{NO_2^-*})$ becomes increasingly
10 negative up to Ni, then increases for Co and Fe. Assuming the BEP relationship holds for
11 electrochemical reduction of nitrite to nitric oxide,⁴⁴ a more negative $\Delta(G_{NO^*} - G_{NO_2^-*})$
12 would then correspond to a lower activation barrier, increasing the preference towards nitrite
13 reduction to nitric oxide (and possibly further to ammonium) over desorption.

14

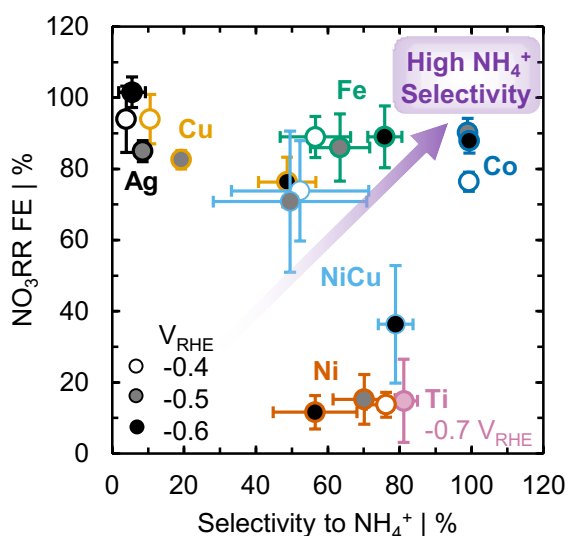
15 4.2.3. Role of electronic structure on selectivity towards ammonium

16 Informed by results from the Ni-Cu system (Figure 4) and theoretical calculations (Figure
17 5), we expand our study to consider the role of TM electronic structure (work function²⁹ and
18 E_d vs E_F ³⁰) and H^{*} affinity (H chemisorption energy²⁶) on NO₃RR FE and selectivity to
19 ammonium. We focus our discussion on potentials with nominal competition between HER
20 and NO₃RR (-0.4, -0.5, and -0.6 V_{RHE}; Figures 6 and 7), with data for additional potentials

1 provided as Figures S16 and S17 and Table S2.

2 Considering NO₃RR FE and ammonium selectivity graphically provides a simple means
3 to identify promising electrocatalysts (Figure 6), which appear increasingly towards the upper-
4 right. TMs such as Cu and Ag, while demonstrating appreciable NO₃RR FE, provide poor
5 selectivity to ammonium. At increasingly cathodic potentials, selectivity towards ammonium
6 does increase for these TMs, though at the cost of NO₃RR FE (Figures S16 and S17).
7 Alternatively, TMs such as Ni and Ti demonstrate the opposite behavior: providing high
8 selectivity towards ammonium with low NO₃RR FE. Optimally, Fe and (in particular) Co
9 demonstrate both appreciable NO₃RR FE and selectivity towards ammonium.

10



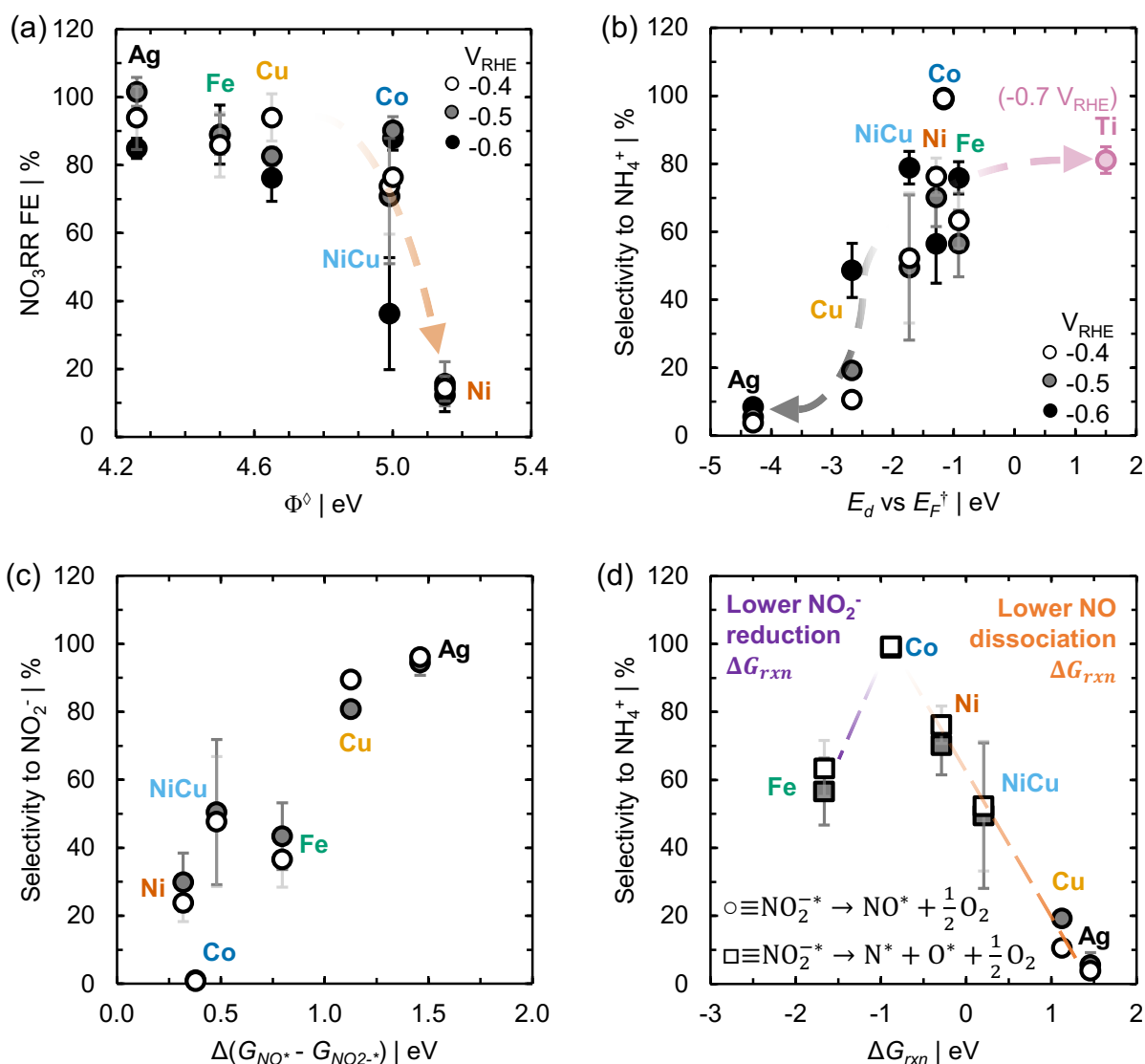
11

12 Figure 6. NO₃RR FE against selectivity to ammonium for a series of TM foils, measured in stirred 0.1 M
13 Na_xH_{3-x}PO₄ with 0.1 M NaNO₃ by 85% iR-corrected chronoamperometry to 0.2 e⁻/NO₃⁻ at -0.4, -0.5, and -0.6
14 V_{RHE} (denoted).

15

16 As NO₃RR FE represents electron selectivity between HER and nitrate reduction, it is best

1 described via H^* affinity towards TM surfaces and the associated electronic descriptor of work
2 function (Figure 7a and Figure S20). NO_3RR FE is appreciable (>70%) for TMs with a broad
3 range of work function and low-to-intermediate H chemisorption energy (e.g. Ag, Cu, Co, Fe),
4 but drops for TMs with either high work function (e.g. Ni, Figure 7a) or high H chemisorption
5 energy (e.g. Ti, Figure S20). Ni (and $Ni_{0.68}Cu_{0.32}$) has the greatest work function, and
6 consequently greatest HER activity (Figure S3),²⁸ of the TMs investigated here, demonstrating
7 poor NO_3RR FE due to facile H-H coupling kinetics. In contrast, low work function Ti has the
8 strongest H chemisorption energy, providing H^* -saturated surfaces that impede nitrate
9 adsorption and/or hydrogen bond formation kinetics (i.e. PCET or hydrogenation).^{26,28,38} The
10 dependence of nitrate rate order on $\Delta G_{H^*} - \Delta G_{NO_3^-}$ discussed in Section 4.1.1 may provide
11 additional context for understanding the relationship between NO_3RR FE and work function
12 as a future direction for the field. Differences in NO_3RR FE are expected to be more
13 pronounced for lower nitrate concentrations typical of e.g. groundwater (~1.5 mM).^{6,7,11,23,45}
14



1
2 Figure 7. (a) NO₃RR FE against work function and (b) selectivity towards ammonium against E_d vs E_F for
3 denoted TM foils measured by 85% iR-corrected chronoamperometry to 0.2 e⁻/NO₃⁻ at select potentials (-0.4,
4 -0.5, and -0.6 V_{RHE}; denoted), except for Ti where -0.7 V_{RHE} is used to obtain sufficient current. Lines to guide
5 the eye. Ti is excluded from (a) due to uncertainties in work function^{29,46} and surface termination (e.g. oxidation
6 state or presence of hydrides),^{37,38} but is included in Figure S20 for reference. (c) Selectivity to nitrite at -0.4 and
7 -0.5 V_{RHE} against calculated reaction free energy for nitrite reduction to nitric oxide. (d) Selectivity to
8 ammonium at -0.4 and -0.5 V_{RHE} against calculated reaction free energies of nitrite to nitric oxide (circles) and
9 dissociated N* and O* adatoms (squares), with lines to guide the eye. Error bars denote one standard deviation of
10 the average of at least three (n = 3) separate measurements. Potential-dependent average and standard deviation
11 of selectivity to ammonium for Co overlaps within the size of the symbols used (see Table S2). [†]Data for work
12 function adapted from Ref. 29 and E_d vs E_F from Ref. 30, with values (a,b) for Ni_{0.68}Cu_{0.32} interpolated from
13 literature values for Ni and Cu.

14

1 We next consider the role of TM E_d vs E_F on selectivity towards ammonium (Figure 7b).
2 For TMs with E_d well below E_F (e.g. Cu, Ag) selectivity towards ammonium is very low
3 (typically <20%), though increases with H^* coverage under more cathodic applied potentials
4 (Figures S16 and S17). In contrast, selectivity towards ammonium is nominally high for E_d
5 approaching E_F (e.g. Ni, Co, Fe), remaining high for TMs with E_d well above E_F (e.g. Ti). This
6 observation can be explained by the d-band model:^{30,47,48} the antibonding molecular orbital
7 formed between adsorbed nitric oxide and the TM surface becomes increasingly unoccupied
8 as E_d approaches and overcomes E_F , manifesting as stronger binding (more negative ΔG_{NO^*})
9 and a preference towards dissociative adsorption ($\Delta G_{N^*+O^*} < G_{NO^*}$, Figure 5). Increased
10 ammonium selectivity for TMs that favor NO dissociation leads us to propose that N^*
11 selectively forms ammonium at the potentials considered here. While the d-band model
12 includes an adsorption energy penalty proportional to the overlap integral squared (V_{ad}^2), we
13 find tabulated values of V_{ad}^2 do not describe well the trends in either NO_3RR FE (Figure S20)
14 or selectivity towards ammonium (Figure S21), suggesting E_d vs E_F predominates this
15 description.

16 While the d-band model provides a first approximation for understanding trends in
17 ammonium selectivity, the ammonium selectivity of Co is exceptionally high (>95%) across
18 the range of potentials measured here (-0.2 to -0.7 V_{RHE} ; Figures S16 and S17) compared to
19 materials of similar E_d vs E_F . To better understand the exceptional ammonium selectivity of Co
20 we consider the calculated reaction free energies of nitrite reduction to nitric oxide and its

1 further dissociation (Figure 7c,d). Selectivity to nitrite nominally decreases as $\Delta(G_{NO^*} -$
2 $G_{NO_2^-})$ decreases (Figure 7c). However, while nitrite reduction is more favorable on Ni than
3 Co, Ni demonstrates a poorer ammonium selectivity than Co. In this case, Ni has a much lower
4 driving force for nitric oxide dissociation than Co (Figure 5b), where we hypothesize N^*
5 selectively reduces to ammonium at the potentials considered here. In contrast, while nitric
6 oxide dissociation is more favorable on Fe compared to Co, nitrite reduction on Fe is less
7 favorable (Figure 5b), resulting in greater nitrite selectivity. This explanation produces a
8 Sabatier-like trend where ammonium selectivity is determined by the free energy of nitrite
9 reduction to either nitric oxide or dissociated N^* (Figure 7d): materials with insufficient driving
10 force for either nitric oxide dissociation (e.g. Ag, Cu, $Ni_{0.68}Cu_{0.32}$, Ni; Figure 5b) or nitrite
11 reduction (e.g. Fe) provide sub-optimal ammonium selectivity. Thus, Co represents an
12 optimum where nitric oxide is bound strong enough to prefer dissociation while still
13 maintaining an appreciable driving force for nitrite reduction.

14 Coupled with our broader understanding of design principles across the range of TMs
15 considered here, these findings suggest that the work function, H chemisorption energy, and E_d
16 vs E_F of Co may serve as optimal catalyst activity and ammonium selectivity design targets.
17 Development of materials spanning the phase space around Co (e.g. $Ni_{1-x}Fe_x$, $Co_{1-x}Fe_x$ or
18 $Co_{1-x}Ni_x$ alloys) may provide a more discrete understanding of this local optimum electronic
19 structure while shifting towards catalysts with greater earth abundance.⁴⁹ Further, the onset
20 potential of NO_3RR on Co could be enhanced by alloying with other highly-active TMs (e.g.

1 $\text{Co}_{1-x}\text{Cu}_x$ alloys),⁷ pairing with metal oxides with greater nitrate affinities,¹¹ or tailoring cation
2 composition and strength within the electrolyte.⁵⁰

3

4 **5. Conclusions**

5 We have investigated the NO_3RR on a series of polycrystalline TM foils in neutral,
6 buffered (0.1 M $\text{Na}_x\text{H}_{3-x}\text{PO}_4$) electrolyte, identifying physicochemical parameters that govern
7 both activity and selectivity towards ammonium. Motivated by periodic trends in H^* affinities
8 and NO_3RR mass-transfer limited potentials, we derived a microkinetic model describing rate-
9 limiting nitrate reduction to nitrite by a combination of hydrogenation and PCET. Potential-
10 dependent nitrate rate order manifests from a competitive adsorption between H^* and nitrate,
11 and is well described in our microkinetic model by the material-dependent $\Delta G_{\text{H}^*} - \Delta G_{\text{NO}_3^-}$.

12 NO_3RR FE originates from competition with HER and is thus well described by HER
13 activity descriptors: high work function TMs demonstrate appreciable HER activity at the
14 detriment of NO_3RR FE, while FE is limited on TMs binding H^* strongly. DFT calculations
15 demonstrate an increasing preference for nitric oxide binding and subsequent dissociation as
16 E_d approaches E_F , commensurate with increasing ammonium selectivity, reaching a maximum
17 for Co. However, selectivity decreases for Fe, attributed to reduced driving force for nitrite
18 reduction to nitric oxide. These results identify competing design considerations – linking
19 electronic structure to mechanistic selectivity-limiting steps – offering strategies to improve
20 existing catalysts and design new alloy compositions for NO_3RR to ammonium.

1 **6. Acknowledgments**

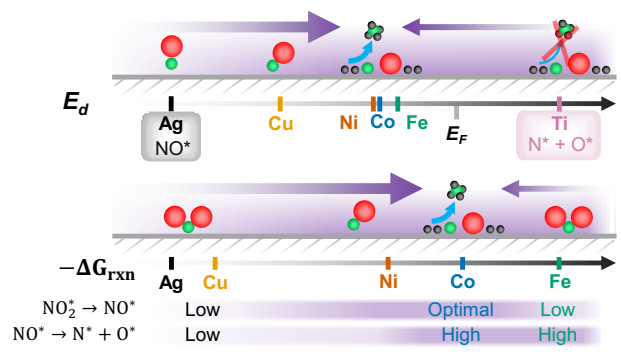
2 K.A.S. acknowledges support from the Oregon State University as a Callahan
3 Faculty Scholar. R.M. acknowledges funding from the Pete and Rosalie Johnson
4 Internship Program. O.Q.C. acknowledges funding from the U.S. DOE SCGSR
5 program, administered by the Oak Ridge Institute for Science and Education for the
6 DOE under contract number DE-SC0014664. H.K.K.N. acknowledges support from the
7 National Science Foundation under Grant No. 1665287. Part of this research was
8 performed via Tahoma allocation on a project award 51428 from the Environmental
9 Molecular Sciences Laboratory, a DOE Office of Science User Facility sponsored by
10 the Biological and Environmental Research program under Contract No. DE-AC05-
11 76RL01830.

1 7. References

- 2 1. Maura, A., Haowei, W. & Upmanu, L. National trends in drinking water quality violations. *Proc. Natl.*
3 *Acad. Sci.* **115**, 2078–2083 (2018).
- 4 2. Battye, W., Aneja, V. P. & Schlesinger, W. H. Is nitrogen the next carbon? *Earth's Futur.* **5**, 894–904 (2017).
- 5 3. Ammonia: zero-carbon fertiliser, fuel and energy storage. *R. Soc.* 1–40 (2020).
- 6 4. Comer, B. M. *et al.* Prospects and Challenges for Solar Fertilizers. *Joule* **3**, 1578–1605 (2019).
- 7 5. Werth, C. J., Yan, C. & Troutman, J. P. Factors Impeding Replacement of Ion Exchange with
8 (Electro)Catalytic Treatment for Nitrate Removal from Drinking Water. *ACS ES&T Eng.* **1**, 6–20 (2021).
- 9 6. Li, J. *et al.* Efficient Ammonia Electrosynthesis from Nitrate on Strained Ruthenium Nanoclusters. *J. Am.*
10 *Chem. Soc.* **142**, 7036–7046 (2020).
- 11 7. Wang, Y. *et al.* Enhanced Nitrate-to-Ammonia Activity on Copper–Nickel Alloys via Tuning of
12 Intermediate Adsorption. *J. Am. Chem. Soc.* **142**, 5702–5708 (2020).
- 13 8. van Langevelde, P. H., Katsounaros, I. & Koper, M. T. M. Electrocatalytic Nitrate Reduction for
14 Sustainable Ammonia Production. *Joule* **5**, 290–294 (2021).
- 15 9. Dima, G. E., Rosca, V. & Koper, M. T. M. Role of germanium in promoting the electrocatalytic reduction
16 of nitrate on platinum: An FTIR and DEMS study. *J. Electroanal. Chem.* **599**, 167–176 (2007).
- 17 10. Wang, Z., Richards, D. & Singh, N. Recent discoveries in the reaction mechanism of heterogeneous
18 electrocatalytic nitrate reduction. *Catal. Sci. Technol.* **11**, 705–725 (2021).
- 19 11. Carvalho, O. Q. *et al.* Role of oxide support in electrocatalytic nitrate reduction on Cu. *Electrochem. Sci.*
20 *Adv.* Under Review (2022).
- 21 12. Pérez-Gallent, E., Figueiredo, M. C., Katsounaros, I. & Koper, M. T. M. Electrocatalytic reduction of
22 Nitrate on Copper single crystals in acidic and alkaline solutions. *Electrochim. Acta* **227**, 77–84 (2017).
- 23 13. Liu, H. *et al.* Electrocatalytic Nitrate Reduction on Oxide-Derived Silver with Tunable Selectivity to
24 Nitrite and Ammonia. *ACS Catal.* **11**, 8431–8442 (2021).
- 25 14. Bouzek, K., Paidar, M., Sadílková, A. & Bergmann, H. Electrochemical reduction of nitrate in weakly
26 alkaline solutions. *J. Appl. Electrochem.* **31**, 1185–1193 (2001).
- 27 15. Fox, C. M. & Breslin, C. B. Electrochemical formation of silver nanoparticles and their applications in
28 the reduction and detection of nitrates at neutral pH. *J. Appl. Electrochem.* **50**, 125–138 (2020).
- 29 16. Duca, M., van der Klugt, B. & Koper, M. T. M. Electrocatalytic reduction of nitrite on transition and
30 coinage metals. *Electrochim. Acta* **68**, 32–43 (2012).
- 31 17. de Vooy, A. C. A., Koper, M. T. M., van Santen, R. A. & van Veen, J. A. R. Mechanistic Study on the
32 Electrocatalytic Reduction of Nitric Oxide on Transition-Metal Electrodes. *J. Catal.* **202**, 387–394 (2001).
- 33 18. Kuwabata, S., Uezumi, S., Tanaka, K. & Tanaka, T. Assimilatory and dissimilatory reduction of nitrate
34 and nitrite with a tris(tetrabutylammonium)
35 nonakis(benzenethiolato)octasulfidohexaferratedimolybdate(3-) modified glassy-carbon electrode in
36 water. *Inorg. Chem.* **25**, 3018–3022 (1986).
- 37 19. Ko, B. H., Hasa, B., Shin, H., Zhao, Y. & Jiao, F. Electrochemical Reduction of Gaseous Nitrogen Oxides
38 on Transition Metals at Ambient Conditions. *J. Am. Chem. Soc.* **144**, 1258–1266 (2022).
- 39 20. Foster, S. L. *et al.* Catalysts for nitrogen reduction to ammonia. *Nat. Catal.* **1**, 490–500 (2018).

- 1 21. Dahl, S., Logadottir, A., Jacobsen, C. J. H. & Nørskov, J. K. Electronic factors in catalysis: the volcano
2 curve and the effect of promotion in catalytic ammonia synthesis. *Appl. Catal. A Gen.* **222**, 19–29 (2001).
- 3 22. Deng, X., Yang, Y., Wang, L., Fu, X.-Z. & Luo, J.-L. Metallic Co Nanoarray Catalyzes Selective NH₃
4 Production from Electrochemical Nitrate Reduction at Current Densities Exceeding 2 A cm⁻². *Adv. Sci.* **8**,
5 2004523 (2021).
- 6 23. Kani, N. C. *et al.* Solar-driven electrochemical synthesis of ammonia using nitrate with 11% solar-to-fuel
7 efficiency at ambient conditions. *Energy Environ. Sci.* **14**, 6349–6359 (2021).
- 8 24. Katsounaros, I., Dortsiou, M. & Kyriacou, G. Electrochemical reduction of nitrate and nitrite in simulated
9 liquid nuclear wastes. *J. Hazard. Mater.* **171**, 323–327 (2009).
- 10 25. Nguyen, T. T. P., Do, B. K. D., Bui, N. N., Pham, M. A. & Nguyen, T. V. Selectiveness of Copper and
11 Polypyrrole Modified Copper Electrodes for Nitrate Electroreduction: A Comparative Study and
12 Application in Ground Water. *ECS Trans.* **53**, 41–52 (2013).
- 13 26. Nordlander, P., Holloway, S. & Nørskov, J. K. Hydrogen adsorption on metal surfaces. *Surf. Sci.* **136**, 59–
14 81 (1984).
- 15 27. Nørskov, J. K. *et al.* Trends in the Exchange Current for Hydrogen Evolution. *J. Electrochem. Soc.* **152**,
16 J23 (2005).
- 17 28. Trasatti, S. Work function, electronegativity, and electrochemical behaviour of metals: III. Electrolytic
18 hydrogen evolution in acid solutions. *J. Electroanal. Chem. Interfacial Electrochem.* **39**, 163–184 (1972).
- 19 29. Michaelson, H. B. The work function of the elements and its periodicity. *J. Appl. Phys.* **48**, 4729–4733
20 (1977).
- 21 30. Hammer, B. & Nørskov, J. K. Theoretical surface science and catalysis—calculations and concepts. *Adv.*
22 *Catal.* **45**, 71–129 (2000).
- 23 31. Monteiro, M. C. O., Liu, X., Hagedoorn, B. J. L., Snabilié, D. D. & Koper, M. T. M. Interfacial pH
24 Measurements Using a Rotating Ring-Disc Electrode with a Voltammetric pH Sensor. *ChemElectroChem*
25 **9**, e202101223 (2022).
- 26 32. Krishtalik, L. I. Hydrogen Overvoltage and Adsorption Phenomena. Part III. Effect of the Adsorption
27 Energy of Hydrogen on Overvoltage and the Mechanisms of the Cathodic Process. in *Advances in*
28 *electrochemistry and electrochemical engineering, Volume 7* (eds. Delahay, P. & Tobias, C. W.)
29 (Interscience Publishers, 1970).
- 30 33. Shinagawa, T., Garcia-Esparza, A. T. & Takanabe, K. Insight on Tafel slopes from a microkinetic analysis
31 of aqueous electrocatalysis for energy conversion. *Sci. Rep.* **5**, 13801 (2015).
- 32 34. Singh, N. *et al.* Aqueous phase catalytic and electrocatalytic hydrogenation of phenol and benzaldehyde
33 over platinum group metals. *J. Catal.* (2020) doi:10.1016/j.jcat.2019.12.034.
- 34 35. Brown, W. A. & King, D. A. NO Chemisorption and Reactions on Metal Surfaces: A New Perspective. *J.*
35 *Phys. Chem. B* **104**, 2578–2595 (2000).
- 36 36. Bligaard, T. *et al.* The Brønsted–Evans–Polanyi relation and the volcano curve in heterogeneous catalysis.
37 *J. Catal.* **224**, 206–217 (2004).
- 38 37. Thomas, N. T. & Nobe, K. Kinetics of the Hydrogen Evolution Reaction on Titanium. *J. Electrochem.*
39 *Soc.* **117**, 622 (1970).
- 40 38. Liu, M. J. *et al.* Catalytic Performance and Near-Surface X-ray Characterization of Titanium Hydride

- 1 Electrodes for the Electrochemical Nitrate Reduction Reaction. *J. Am. Chem. Soc.* **144**, 5739–5744 (2022).
- 2 39. Hammer, B. Special Sites at Noble and Late Transition Metal Catalysts. *Top. Catal.* **37**, 3–16 (2006).
- 3 40. Liu, J.-X., Richards, D., Singh, N. & Goldsmith, B. R. Activity and Selectivity Trends in Electrocatalytic
4 Nitrate Reduction on Transition Metals. *ACS Catal.* **9**, 7052–7064 (2019).
- 5 41. Logadottir, A. *et al.* The Brønsted–Evans–Polanyi Relation and the Volcano Plot for Ammonia Synthesis
6 over Transition Metal Catalysts. *J. Catal.* **197**, 229–231 (2001).
- 7 42. Patra, A., Jana, S., Constantin, L. A., Chiodo, L. & Samal, P. Improved transition metal surface energies
8 from a generalized gradient approximation developed for quasi two-dimensional systems. *J. Chem. Phys.*
9 **152**, 151101 (2020).
- 10 43. Abild-Pedersen, F. *et al.* Scaling Properties of Adsorption Energies for Hydrogen-Containing Molecules
11 on Transition-Metal Surfaces. *Phys. Rev. Lett.* **99**, 16105 (2007).
- 12 44. Akhade, S. A., Nidzyn, R. M., Rostamikia, G. & Janik, M. J. Using Brønsted-Evans-Polanyi relations to
13 predict electrode potential-dependent activation energies. *Catal. Today* **312**, 82–91 (2018).
- 14 45. Pennino, M. J., Compton, J. E. & Leibowitz, S. G. Trends in Drinking Water Nitrate Violations Across the
15 United States. *Environ. Sci. Technol.* **51**, 13450–13460 (2017).
- 16 46. Fukuda, Y., Elam, W. T. & Park, R. L. Absolute 2p_{3/2} core binding energies and work functions of 3d
17 transition-metal surfaces. *Phys. Rev. B* **16**, 3322–3329 (1977).
- 18 47. Shiotari, A., Koshida, H. & Okuyama, H. Adsorption and valence electronic states of nitric oxide on metal
19 surfaces. *Surf. Sci. Rep.* **76**, 100500 (2020).
- 20 48. Spivey, T. D. & Holewinski, A. Selective Interactions between Free-Atom-like d-States in Single-Atom
21 Alloy Catalysts and Near-Frontier Molecular Orbitals. *J. Am. Chem. Soc.* **143**, 11897–11902 (2021).
- 22 49. Vesborg, P. C. K. & Jaramillo, T. F. Addressing the terawatt challenge: scalability in the supply of chemical
23 elements for renewable energy. *RSC Adv.* **2**, 7933–7947 (2012).
- 24 50. Katsounaros, I. & Kyriacou, G. Influence of the concentration and the nature of the supporting electrolyte
25 on the electrochemical reduction of nitrate on tin cathode. *Electrochim. Acta* **52**, 6412–6420 (2007).
- 26
- 27



For graphical abstract only

1